CHINESE OPTICS LETTERS

Vol. 19, No. 10 | October 2021

# Dual-band independent phase control based on high efficiency metasurface [Invited]

Jinxing Li (李金星)[1], Yueyi Yuan (袁乐贻)[1], Qun Wu (吴 群)[1], Shah Nawaz Burokur[2], and Kuang Zhang (张 狂)[1*]

[1] Department of Microwave Engineering, Harbin Institute of Technology, Harbin 150001, China

[2] LEME, UPL, Université Paris Nanterre, F92410 Ville d'Avray, France

*Corresponding author: zhangkuang@hit.edu.cn

Received February 17, 2021 | Accepted May 14, 2021 | Posted Online August 18, 2021

A general method to realize arbitrary dual-band independent phase control is proposed and demonstrated in this paper. A double-layered C-shape reflective meta-atom is designed to realize independent phase control with high efficiency. As a proof of concept, we propose two functional metasurfaces in the microwave region; the first metasurface performs beam steering in different directions, and the second metasurface generates achromatic beam steering at two distinct frequencies. Both simulation and measurement results agree well with the theoretical pre-setting. The maximum measured efficiency is 88.7% and 92.3% at 6.8 GHz and 8.0 GHz, respectively, for one metasurface, and 91.0% and 89.8% at 6.9 GHz and 8.6 GHz, respectively, for the other.

**Keywords:** dual-band; independent phase control; microwave; metasurface; high efficiency; reflection; geometric phase.
**DOI:** 10.3788/COL202119.100501

## 1. Introduction

In the trend of developments in science and technology, higher requirements for the manipulation of electromagnetic (EM) waves are put forward. Therefore, the manipulation of EM waves has been established as an interesting research topic for a long time. In recent years, metasurfaces, which are thin arrays of periodic or quasi-periodic subwavelength elements (or meta-atoms), have developed rapidly and comprehensively from microwave to optical region for their outstanding ability to tailor EM waves[1–3]. Besides, the low profile, light weight, and easy fabrication features are favorable for practical applications. As a result, many research achievements have been obtained in the field of metasurfaces, such as invisible cloaks[4–6], orbital angular momentum (OAM) beam generators[7–11], hologram imagers[12–18], achromatic lenses[19–21], reconfigurable wavefront shaping metasurfaces[22–26], and other multifunctional metasurfaces[27–46].

In order to improve the utilization of a single metasurface, integrating multiple functionalities into a single metasurface is of great interest. Various functionality integrating methods have been proposed, which are based on the decoupling mechanisms of EM intrinsic characteristics, such as frequency[27–30], polarization[31–39], incidence angle[40–43], and propagating direction[44–46]. Particularly, frequency multiplexing metasurfaces allow us to increase the utilization of the frequency domain, which can effectively improve the service quality of communication systems. However, there are many issues that hinder the practical application of frequency multiplexing metasurfaces, primarily including low efficiency and inadequate stability. Therefore, high efficiency frequency multiplexing metasurfaces are highly desirable for potential implementation in real-life applications.

In this paper, we propose a general method to realize independent phase control in two arbitrary frequency bands. The main goal is to control the phase difference at the two arbitrary frequencies with full phase coverage and impose a frequency-independent phase control mechanism in order to decouple the phase responses at the two-target frequency. Here, we design a double-layered C-shape reflective meta-atom with geometric phase principle, which can realize the proposed dual-band independent phase control method with high efficiency. To experimentally verify the characteristics of the proposed meta-atom design, three periodic structures, each composed of a periodic arrangement of similar cells, are fabricated and measured. The measurement results of the three structures are in good agreement with simulations, validating the fact that the designed meta-atom is indeed able to independently control phase at two frequencies with high efficiency.

Furthermore, as a beam manipulation functionality proof-of-concept, two dual-band metasurfaces are designed, simulated, and measured. The first metasurface (MTS1) can steer a beam to different directions at 6.6 GHz and 8.4 GHz, and the second one achromatically steers a beam to the same direction at 6.6 GHz and 8.4 GHz. Simulation and experimental results

indicate that the two metasurfaces can effectively achieve the theoretical predefined functionalities. Efficiencies higher than 87% are achieved in both simulations and measurements at the desired frequencies. The proposed scheme for dual-band independent phase control provides a new scheme for practical applications in modern wireless communication systems.

## 2. Principle and Meta-Atom Design

To achieve dual-band independent phase control, we propose a method to decouple the phase of a meta-atom at two arbitrary frequencies. Hence, we are able to establish a library of meta-atoms showing a full phase range at the two selected frequencies. Based on this meta-atoms' library, two distinct selected functionalities can be imposed at independent operating frequencies. The proposed method is realized in two steps. The first step consists of introducing a frequency-independent phase control mechanism to manipulate the phase of the meta-atoms. The second step then consists of making the phase difference of the meta-atom at the two selected frequencies vary in the range of $-\pi$ to $\pi$. Based on these two steps, the phase of a meta-atom at two different frequencies can be independently controlled.

Geometric phase is a frequency-independent phase control mechanism[31], which has been widely used due to its implementation simplicity. Geometric phase can introduce a frequency-independent phase shift $\Delta\varphi_{gp} = 2\sigma\theta$ into the output wave, with $\sigma = 1$ or $-1$ corresponding to the input right-handed circular polarization (RCP) or left-handed circular polarization (LCP) wave, and $\theta$ being the angular orientation of the meta-atom. Here, we apply geometric phase mechanisms to accomplish design step 1. Therefore, if we can find a group of geometric phase meta-atoms satisfying design step 2, dual-band independent phase control can be realized. Here, we use an incident RCP plane wave propagating toward the $-z$ direction, and the spin state of the output EM field is opposite to the input one. Meanwhile, the reflected output wave propagates toward the $+z$ direction, opposite to the input wave direction. Therefore, since the spin state and propagating direction of the output wave are both opposite to those of the input wave, according to the definition of the circular polarization wave, the polarization of the output wave is still RCP. As such, the reflective meta-atom imposes a geometric phase to the co-polarized reflected wave since its spin state of EM is opposite to that of the input wave.

Next, it is important to control the phase of the reflection coefficient. The EM response of the linear-polarized reflected wave can be characterized by the reflection Jones matrix in the linear polarization basis, which is expressed as

$$R = \begin{pmatrix} r_{xx} & r_{xy} \\ r_{yx} & r_{yy} \end{pmatrix} = \begin{pmatrix} |r_{xx}|e^{j\varphi_{xx}} & |r_{xy}|e^{j\varphi_{xy}} \\ |r_{yx}|e^{j\varphi_{yx}} & |r_{yy}|e^{j\varphi_{yy}} \end{pmatrix}, \quad (1)$$

where $x$ and $y$ represent $x$ and $y$ polarization, respectively. $r_{xx}$ and $r_{yx}$ are the co- and cross-polarized reflection coefficients, respectively, under $x$-polarized wave illumination. Similarly, $r_{yy}$ and $r_{xy}$ are the co- and cross-polarized reflected components, respectively, under $y$-polarized wave illumination. For a circular polarization basis, the co-polarized RCP wave component of the reflection Jones matrix can be expressed as

$$r_{++} = \frac{1}{2}[r_{xx} - r_{yy} + j(r_{xy} + r_{yx})], \quad (2)$$

where the '+' sign represents RCP. Equation (2) indicates that the cross-polarization reflection coefficient of linear polarization can be used to control the complex reflection coefficient $r_{++}$. If $r_{xy}$ and $r_{yx}$ at two frequencies can be controlled independently, it is then possible to make the phase difference of $r_{++}$ at two frequencies vary arbitrarily in the range of $-\pi$ to $\pi$.

To realize design step 2 practically, a double-layered C-shape reflective meta-atom is proposed, as shown in Fig. 1. The meta-atom consists of two low loss F4BM350 dielectric substrates ($\varepsilon_r = 3.5$ and $\tan\delta = 0.001$) with the same thickness $h$, two layers of C-shape metal strips with radius $r$, and a metal ground plane. The arc-angle of the top layer and middle layer C-shape strips is $\alpha_1$ and $\alpha_2$, respectively. $\theta_1$ and $\theta_2$ are the anticlockwise rotation angles of the C-shape strips on the top and middle layers, respectively, which can be considered as the angle between the symmetry axis and $x$ axis. The meta-atoms are arranged in a uniform hexagonal lattice with a side length $p$. Through tailoring the geometrical parameters of the meta-atom, the EM response of the reflected wave can be controlled as desired. The geometrical parameters are optimized through simulations in order to achieve high efficiency together with broad bandwidth. The fixed parameters of the designed structure are $p = 6$ mm, $r = 3$ mm, $h = 2$ mm, $w = 0.2$ mm, $\alpha_1 = 210°$, and $\alpha_2 = 200°$. Rotation angles $\theta_1$ and $\theta_2$ are the main parameters used to control the reflection phase of $r_{++}$.

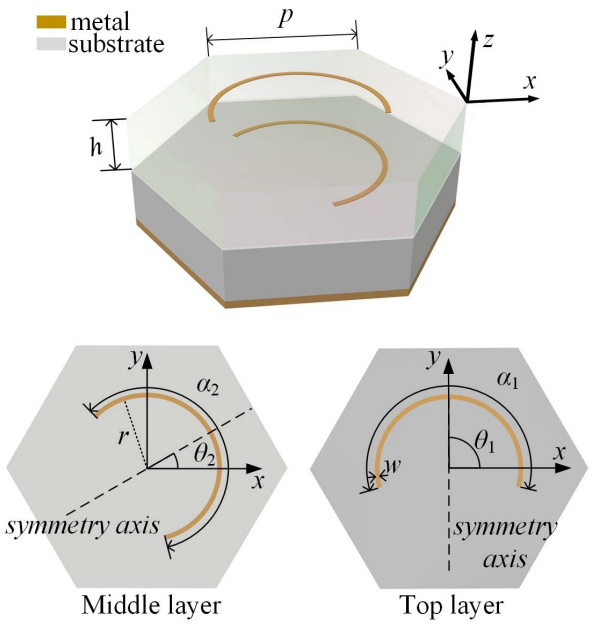


**Fig. 1.** Schematic structures of the proposed meta-atom with the different geometrical details.

Three different unit cells of the considered meta-atom are simulated in an infinite array using periodic boundary conditions, where an RCP plane wave is used as the illuminating incident wave. A perfect electric conductor (PEC) is considered for the metal parts in the simulations. The reflection magnitude and phase of $r_{++}$ for different $\theta_1$ values are shown in Figs. 2(a) and 2(b), respectively. For the considered values of $\theta_1$, the reflection magnitude at 6.6 GHz is above 0.9, while the phase hardly changes. From 8.4 GHz to 9.5 GHz also, the reflection magnitude exhibits high efficiency, but the phase changes over a large range. Therefore, the two frequencies of independent phase control can be selected as $f_1 = 6.6$ GHz and $f_2 \in [8.4, 9.5]$ GHz. To satisfy the Nyquist sampling theorem, the period of the meta-atom must be smaller than half of the shorter wavelength $\lambda_2$. Here, we fix the nearest frequencies $f_1 = 6.6$ GHz and $f_2 = 8.4$ GHz to show dual-band independent phase control.

The three unit cells are each arranged in a separate finite structure of size 200 mm × 200 mm, which are shown in Fig. 3. The three prototypes are fabricated on 35 μm thick copper-cladded F4BM350 dielectric substrates using the classical printed circuit board (PCB) technique and tested to experimentally verify the EM properties obtained from the unit cell simulations. The only different structure parameter of the three structures is the top layer C-shape strip's rotation angle $\theta_1$, which is 0°, 70°, and 180°, respectively. The structures are named as 'S0', 'S70', and 'S180', respectively. The measured amplitude and phase of the reflection coefficient $r_{++}$ presented in Figs. 2(c) and 2(d), respectively. The magnitudes at 6.6 GHz and 8.4 GHz of the three structures are all above 0.9. The phase at 6.6 GHz is quasi-similar in the three cases, while at 8.4 GHz the phases of S0 and S180 are nearly similar, but present a difference of 180° with

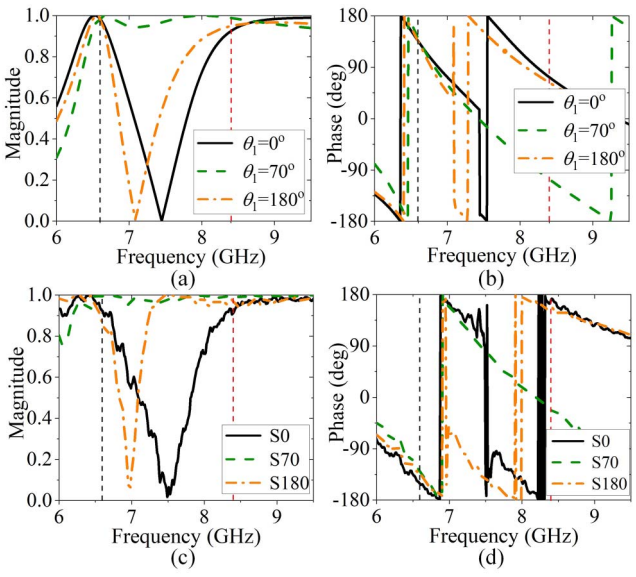


**Fig. 2.** Co-polarized reflection coefficient $r_{++}$ for different values of $\theta_1$. (a) Simulated magnitude, (b) simulated phase, (c) measured magnitude, and (d) measured phase. 6.6 GHz and 8.4 GHz are, respectively, highlighted by the vertical black dashed trace and red dashed trace.

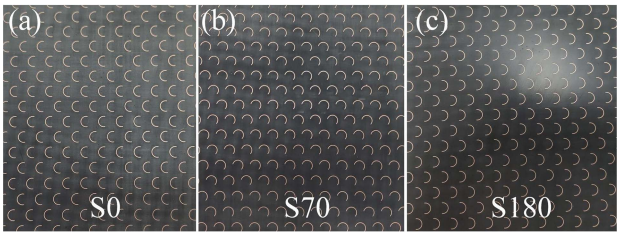


**Fig. 3.** Partial views of the fabricated prototypes. (a) S0, (b) S70, and (c) S180.

that of S70. Therefore, the measurement results of $r_{++}$ are consistent with the corresponding simulation results, proving that the designed meta-atom can manipulate the EM properties at two frequencies in an independent and effective manner.

In order to further describe the operating mechanism of this double-layered structure, the two separate C-shape strips are simulated independently. In the first model, only the middle layer is kept, while for the second model, only the top layer is kept. The $r_{++}$ magnitudes of the two models are shown in Fig. 4(a). The two responses are completely distinct, which indicates that the resonance at two frequencies can be independently manipulated. The middle layer C-shape strip exhibits a sharp resonance at 6.6 GHz, while the top layer C-shape strip shows a broad flat resonance from 8 GHz to 12 GHz.

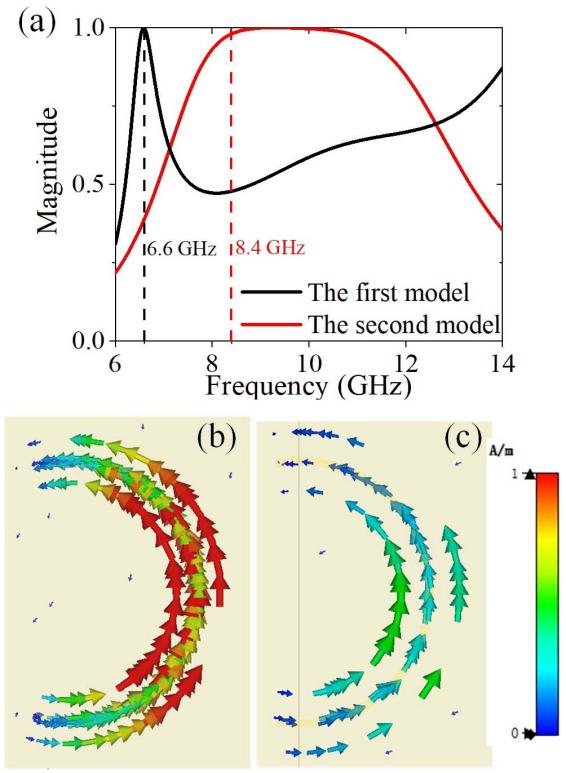


**Fig. 4.** (a) Magnitude of the co-polarized reflection coefficient $r_{++}$ of the top and middle C-strips separately. The black and red traces correspond to the middle and top layer strips, respectively. (b) Normalized current distribution of the middle layer strip at 6.6 GHz. (c) Normalized current distribution of the top layer strip at 8.4 GHz.

Figs. 4(b) and 4(c) show the normalized current distribution of the middle layer at 6.6 GHz and top layer at 8.4 GHz, respectively, where the current strength of the middle layer is much stronger than that of the top layer, which indicates that the resonance at 6.6 GHz is much stronger than the resonance at 8.4 GHz. Through this investigation, we can deduce that the middle layer C-shape strip interacts strongly with an EM wave at 6.6 GHz, and the EM properties of the meta-atom at 6.6 GHz are dominated by this resonance. However, in the frequency band ranging from 8 GHz to 9.5 GHz, the resonance is influenced by both layers of strips simultaneously. Therefore, changing $\theta_1$ with fixed $\theta_2$ can indeed allow us to manipulate the phase of $r_{++}$ at 8.4 GHz, but will slightly affect the phase of $r_{++}$ at 6.6 GHz, which is the key point to control the phase difference at two frequencies.

The phase difference of $r_{++}$ is mainly caused by the different linearly cross-polarized effects at the two frequencies. For this meta-atom, the relation $r_{xy} = r_{yx}$ always holds. Since the angle $\theta_1$ is the main parameter to control the response of $r_{xy}$, the relation between $r_{xy}$ and $\theta_1$ is investigated.

The magnitude and phase responses of $r_{xy}$ for different $\theta_1$ are shown in Figs. 5(a) and 5(b), respectively. At 6.6 GHz, the magnitude of $r_{xy}$ varies in the range of 0 to 0.4, and the phase varies within a narrow range, which causes the magnitude and phase of $r_{++}$ to hardly change at 6.4 GHz for different $\theta_1$. At 8.4 GHz, the magnitude of $r_{xy}$ varies in a wider range from 0 to 1, and the phase presents an obvious difference for the $\theta_1$ range. This means the EM characteristic of $r_{++}$ will change considerably at 8.4 GHz for different $\theta_1$. Therefore, varying $\theta_1$ within a certain range can realize distinct control of $r_{++}$ at two frequencies, making the phase difference vary within the range of $-\pi$ to $\pi$. Therefore, by fixing angle $\theta_2 = 0°$ and gradually increasing angle $\theta_1$ from 0° to 180°, we can manipulate the phase at 8.4 GHz with only a slight change at 6.6 GHz. The responses of $r_{++}$ versus $\theta_1$ are presented in Figs. 6(a) and 6(b), where it can be observed that the phase at 8.4 GHz shifts over a 360° range, but the phase at 6.6 GHz changes only slightly. The phase difference at the two frequencies can vary in the range spanning from −180° to 180°, which satisfies the condition of design step 2. Moreover, the magnitude levels are above 0.9 at both 6.6 GHz and 8.4 GHz. The complex reflection coefficient of the co-polarized wave at two frequencies can be written as $r_{++}(\theta_1, \theta_2, f_i)$, where $i = 1,2$ represents two selected frequencies, and $\theta_1$ and $\theta_2$ are

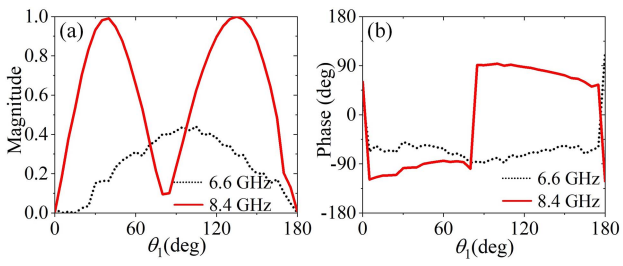


**Fig. 5.** Relation between $r_{xy}$ and $\theta_1$ at 6.6 GHz and 8.4 GHz. (a) Magnitude, (b) phase.

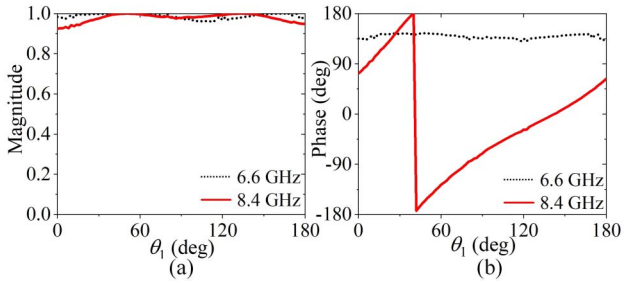


**Fig. 6.** Relations between $r_{++}$ and $\theta_1$ at 6.6 GHz and 8.4 GHz. (a) Magnitude, (b) phase.

independent geometrical parameters of the meta-atom. Now that we know the results of $r_{++}(\theta_1, 0, f_i)$ for $\theta_1 \in [0°,180°]$, we can discretize the phase results of $r_{++}$ at 8.4 GHz with 15° steps and record the corresponding $\theta_1$ of meta-atoms into a structure group in order to accomplish design step 2. Thus, we apply the geometric phase principle to shift the phase with the same value at the two frequencies.

We define a co-rotation angle $\theta_{co}$, which is the anticlockwise rotation angle of the overall structure. According to the geometric phase principle, a $2\theta_{co}$ phase interruption can be introduced into the original phase without affecting the magnitude response of the meta-atom, which is frequency-independent. Gradually increasing $\theta_{co}$ from 0° to 180° enables us to easily accomplish phase decoupling at the two frequencies; here, we increase $\theta_{co}$ of the structure parameter group found in step 1 from 0° to 180° with 7.5° steps. Finally, the phase of $r_{++}$ at 6.6 GHz and 8.4 GHz is decoupled completely, and an orthogonal table with full phase range and discrete 15° phase step at 6.6 GHz and 8.4 GHz is established.

Furthermore, the designed meta-atom can work robustly due to two interesting features. First, the phase is manipulated only by rotating the orientation angle of the C-shape strips. Therefore, the shape and geometrical dimensions of all constituting meta-atoms are similar, making the coupling between neighboring meta-atoms similar. Second, the arrangement of the meta-atoms is a uniform hexagonal lattice that provides high rotation symmetry for meta-atoms. For these two reasons, the robustness of the meta-atom is improved.

## 3. Dual-Band Metasurface Design

The proposed method can control phase independently at the two selected frequencies, which can be applied to realize independent functionalities. As a proof of concept, we design two metasurfaces with different functionalities, which operate under normal RCP incident wave excitation. The schematics of the operating principles of the metasurfaces are shown in Figs. 7(a) and 7(d).

MTS1 is designed to steer the beam to 45° along the $-x$ direction at 6.6 GHz and 15° along the $-y$ direction at 8.4 GHz, respectively. The second metasurface (MTS2) is designed to steer the beam to 30° along the $-x$ direction achromatically at

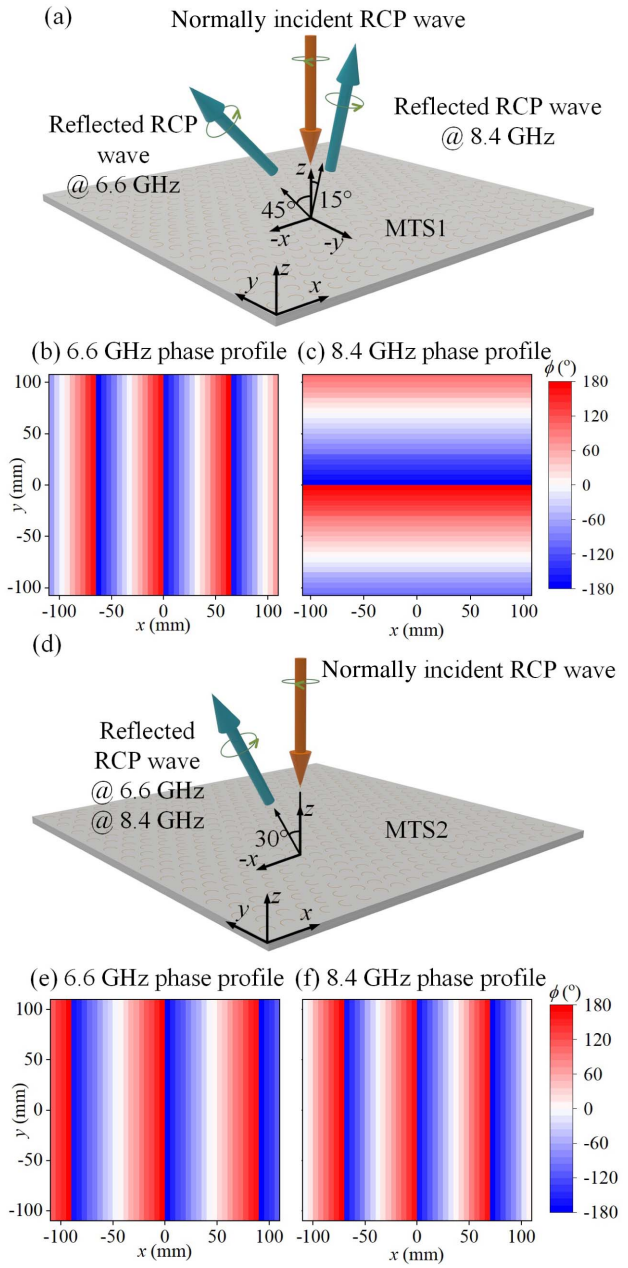


**Fig. 7.** Schematics of the operating principles of (a) MTS1 and (d) MTS2. Phase profiles of MTS1 at (b) 6.6 GHz and (c) 8.4 GHz. Phase profiles of MTS2 at (e) 6.6 GHz and (f) 8.4 GHz.

6.6 GHz and 8.4 GHz. The metasurfaces have a size of 215 mm × 215 mm and a 4.105 mm thickness, and are composed of 460 meta-atoms arranged in a hexagonal lattice. The metasurfaces are constructed with the corresponding meta-atoms and the required phase profiles. Here, the discrete gradient phase profile of beam steering can be expressed as

$$\varphi(\vec{r},f_i) = -\frac{2\pi f_i}{c}\vec{r}\cdot\vec{D}\sin\theta_{bs} + \phi_i, \tag{3}$$

where $\vec{r}$ represents positions on the metasurface, $\vec{D}$ is the unit vector representing the direction of the phase gradient, $\phi_i$ is an arbitrary initial phase value, $\theta_{bs}$ is the beam steering angle toward the direction of the phase gradient, $c$ is the speed of light in vacuum, and $f_i$ is the desired frequency ($i = 1,2$). At the position $\vec{r}$, different frequencies need different phase values, and the required phase at this position can be written as $[\varphi(\vec{r},f_1), \varphi(\vec{r},f_2)]$. From the phase table, the meta-atom that matches the required phase value can be found and used to construct the metasurfaces at the corresponding position. This process is repeated at each position until the metasurface is constructed completely. The design phase profiles of dual-band metasurfaces are shown in Figs. 7(b), 7(c), 7(e), and 7(f).

The two metasurfaces are designed and fabricated. Numerical simulations and experimental measurements are employed to validate the design method of the metasurfaces. The measurement setup and schematic are shown in Fig. 8. The normalized magnitude of the RCP electric field in the far-field region of MTS1 and MTS2 is simulated and measured from 6.1 GHz to 8.9 GHz.

For MTS1, the measured and simulated magnitudes of the RCP electric field in the far-field region in the *xoz* and *yoz* planes at 6.1–8.9 GHz are shown in Fig. 9, which reveal that most of the reflected RCP wave energy is steered to the desired direction in the two frequency bands of interest. Results show that MTS1 performs beam steering on the *xoz* and *yoz* planes at 6.1–7.9 GHz and 7.3–8.9 GHz, respectively. Simulated (measured) beam steering angles are −49° to −38° (−51° to −38°) at 6.1–7.9 GHz and −17° to −14° (−19° to −16°) at 7.2–8.9 GHz, respectively. Both simulated and measured performances agree well with the design goals of −45° at 6.6 GHz and −15° at 8.4 GHz. Since all of the meta-atoms only work precisely and efficiently in the pre-set frequency bands (first band around 6.6 GHz, second band around 8.4 GHz), for the frequency beyond the pre-set frequency band, the corresponding performance would decrease. The steering angle decreases as frequency increases in both bands due to dispersion. Indeed, in Eq. (3), the gradient of phase profile $\nabla\varphi = \partial\varphi(\vec{r},f_i)/\partial\vec{r}$ can be approximated as constant in each working band, and the steering angle can be calculated as $\theta_{bs} = \arcsin(\nabla\varphi c/2\pi f)$, with $f$ being the working frequency.

Figure 10 presents the simulated and measured RCP electric-field data of MTS2 in the *xoz* plane. Simulated (measured) beam steering angles are −35° to −29° (−42° to −28°) at 6.1–8.9 GHz. Both simulated and measured beam steering angles agree well with the theoretical value. As the frequency increases, the beam steering angle decreases at 6.1–7.1 GHz and 7.9–8.9 GHz but increases at 7.1–7.9 GHz. The phase profiles of MTS2 at 6.6 GHz and 8.4 GHz are illustrated in Figs. 7(e) and 7(f), respectively, showing that the phase gradients are in the same direction, but the phase gradient at 8.4 GHz is steeper. Therefore, there is a transition band of phase gradient at 6.6–8.4 GHz, whose phase gradient tendency becomes steeper as the frequency increases, which makes the measured beam steering angle increase within the 7.1 GHz to 7.9 GHz frequency range. Anyway, the beam steering angle variation tendency versus

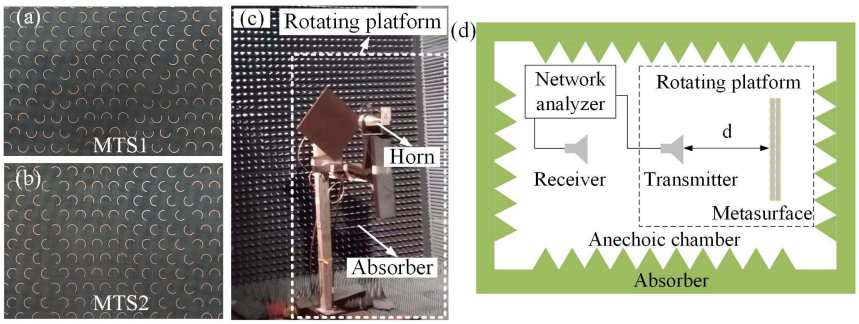


**Fig. 8.** Partial view of the fabricated MTSs. (a) MTS1 and (b) MTS2. (c) Photograph of measurement setup showing the MTS illuminated by a horn antenna. (d) Schematic illustration of the far-field measurement setup in a microwave anechoic chamber.

frequency can still be calculated by Eq. (3), but the phase gradient $\nabla\varphi$ in the transition band cannot be approximated as constant. Overall, the simulated and measured results of the normalized far-field data agree well with each other. The slight discrepancies that can be observed between simulations and measurements are inevitably caused by the fabrication tolerances of the samples and can also be due to the limitation of the measurement setup such as the non-ideal plane wave incidence.

The simulated and measured efficiencies of the reflected RCP waves of MTS1 and MTS2 are shown in Fig. 11, which are calculated as

$$R_{\mathrm{RCP}} = \frac{\int_{-x}^{x}\int_{-y}^{y} E_{R\_\mathrm{RCP}}^2 \mathrm{d}y\mathrm{d}x}{\int_{-x}^{x}\int_{-y}^{y} E_{R\_T}^2 \mathrm{d}y\mathrm{d}x}, \tag{4}$$

where $R_{\mathrm{RCP}}$ is the efficiency of the metasurface, $E_{R\_\mathrm{RCP}}$ is the electric field of the reflected RCP wave, and $E_{R\_T}$ is the total electric field of the reflected wave. The simulated and measured efficiencies at 6.1–8.9 GHz are calculated for both metasurfaces. Both simulated and measured efficiencies of MTS1 and MTS2 are highly consistent with each other. In the band from 6.1 GHz to 7.1 GHz centered at the 6.6 GHz design frequency, the efficiencies of MTS1 and MTS2 are both higher than 80% above 6.7 GHz, and the maximum simulated (measured) efficiencies of MTS1 and MTS2 are 88.3% and 87.8% at 6.9 GHz (88.7% and 91.0% at 6.8 GHz and 6.9 GHz), respectively. In the band from 7.9 GHz to 8.9 GHz centered at the 8.4 GHz design frequency, the efficiency of MTS1 and MTS2 is quite stable, and the maximum simulated (measured) efficiencies of

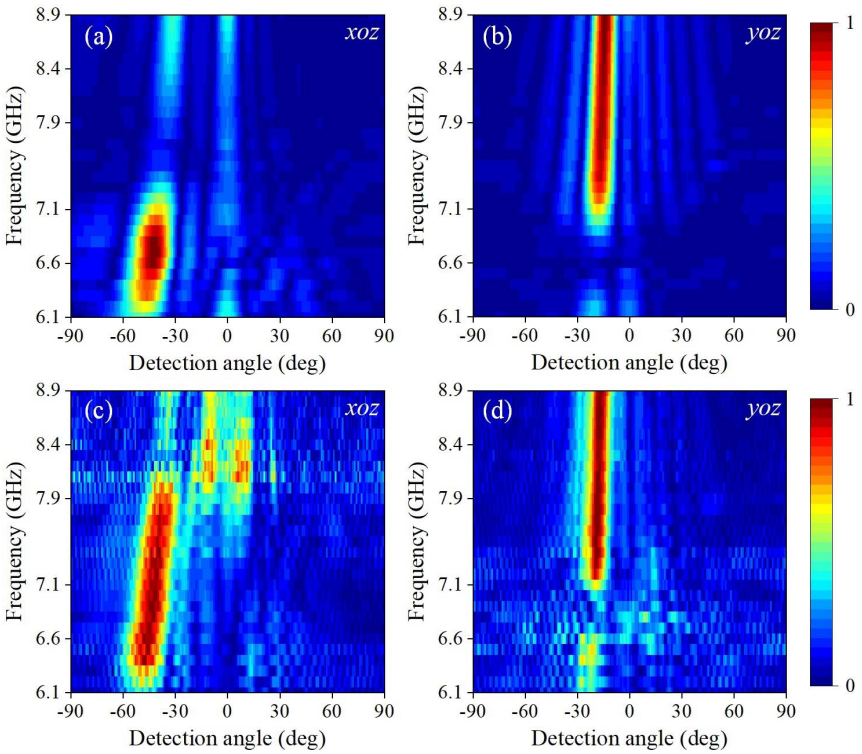


**Fig. 9.** Normalized magnitude of RCP electric field in the far-field region plotted versus detection angle and frequency of MTS1. (a) Simulated and (c) measured results in the *xoz* plane. (b) Simulated and (d) measured results in the *yoz* plane.

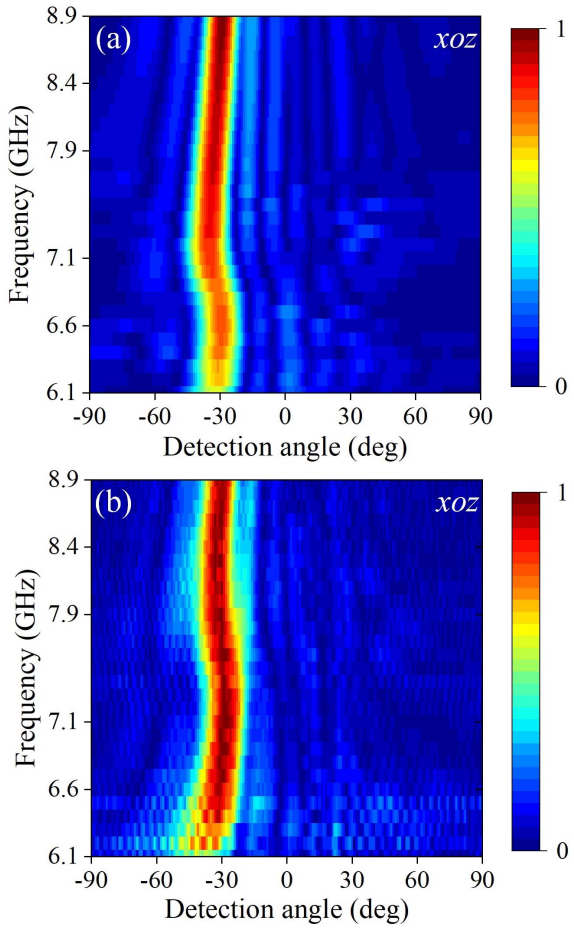


**Fig. 10.** Normalized magnitude of RCP electric field in the far-field region plotted versus detection angle and frequency of MTS2 in the *xoz* plane. (a) Simulated and (b) measured results.

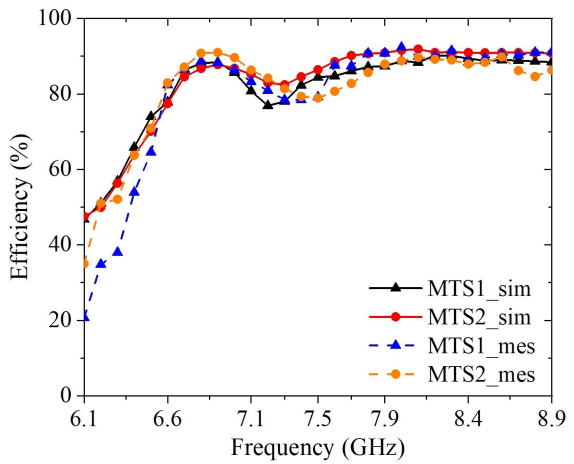


**Fig. 11.** Simulated and measured RCP reflection efficiencies of MTS1 and MTS2.

MTS1 and MTS2 are 90.2% and 91.9% at 8.2 GHz and 8.1 GHz (92.3% and 89.8% at 8 GHz and 8.6 GHz), respectively. Besides, in the band from 7.1 GHz to 7.9 GHz between the two design frequency bands, the efficiency decreases slightly due to the non-uniform amplitude response of all of the meta-atoms used to compose the metasurfaces. In conclusion, the efficiency of MTS1 and MTS2 at 6.7–8.9 GHz is mostly above 80%. The maximum efficiency is around 90%, slightly lower than that of the meta-atom due to some regions on the metasurfaces that cannot perform anomalous reflection correctly.

## 4. Conclusion

To sum up, we propose a general method to realize independent phase control at two arbitrarily chosen frequencies, which is accomplished in two steps. The first step consists of applying a frequency-independent phase control mechanism, which is realized through the geometric phase principle. The second step consists of making the phase difference of $r_{++}$ at two selected frequencies vary in the full $-\pi$ to $\pi$ phase range, which is realized through controlling the cross-polarization response of the linear-polarized wave at the two frequencies. A double-layered C-shape meta-atom is designed to realize the independent phase control at 6.6 GHz and 8.4 GHz with a magnitude above 0.9. As a proof-of-concept, two dual-band metasurfaces with different functionalities are designed, simulated, fabricated, and measured. Both simulation and measurement results show that the beam steering angle of the two metasurfaces agrees well with the design goals at 6.6 GHz and 8.4 GHz. Efficiencies higher than 87% are achieved in both simulations and measurements at the desired frequencies. Such a high efficiency feature is favorable for practical applications. As such, the dual-band independent phase control design method together with the high efficiency meta-atom provides a new option to practical dual-band system applications, particularly in wireless communication systems.

## Acknowledgement

K. Zhang acknowledges the support from National Natural Science Foundation of China (No. 61771172), Open Project of Guangxi Key Laboratory of Wireless Wideband Communication and Signal Processing, and Natural Science Foundation of Heilongjiang Province (No. YQ2020F002).

## References

1. N. F. Yu, P. Genevet, M. A. Kats, F. Aieta, J. P. Tetienne, F. Capasso, and Z. Gaburro, "Light propagation with phase discontinuities: generalized laws of reflection and refraction," Science **334**, 333 (2011).
2. X. Ni, N. K. Emani, A. V. Kildishev, A. Boltasseva, and V. M. Shalaev, "Broadband light bending with plasmonic nanoantennas," Science **335**, 427 (2012).
3. D. Lin, P. Fan, E. Hasman, and M. L. Brongersma, "Dielectric gradient metasurface optical elements," Science **345**, 298 (2014).
4. D. Schurig, J. J. Mock, B. J. Justice, S. A. Cummer, J. B. Pendry, A. F. Starr, and D. R. Smith, "Metamaterial electromagnetic cloak at microwave frequencies," Science **314**, 977 (2006).
5. T. Ergin, N. Stenger, P. Brenner, J. B. Pendry, and M. Wegener, "Three-dimensional invisibility cloak at optical wavelengths," Science **328**, 337 (2010).

6. C. Qian, B. Zheng, Y. Shen, L. Jing, E. Li, L. Shen, and H. Chen, "Deep-learning-enabled self-adaptive microwave cloak without human intervention," Nat. Photon. **14**, 383 (2020).
7. R. C. Devlin, A. Ambrosio, N. A. B. Rubin, J. P. Mueller, and F. Capasso, "Arbitrary spin-to-orbital angular momentum conversion of light," Science **358**, 896 (2017).
8. K. Zhang, Y. Y. Yuan, D. W. Zhang, X. M. Ding, B. Ratni, S. N. Burokur, M. J. Lu, K. Tang, and Q. Wu, "Phase-engineered metalenses to generate converging and non-diffractive vortex beam carrying orbital angular momentum in microwave region," Opt. Express **26**, 1351 (2018).
9. Y. Wang, K. Zhang, Y. Yuan, X. Ding, B. Ratni, S. N. Burokur, and Q. Wu, "Planar vortex beam generator for circularly polarized incidence based on FSS," IEEE Trans. Antennas Propag. **68**, 1514 (2020).
10. F. Bi, Z. Ba, and X. Wang, "Metasurface-based broadband orbital angular momentum generator in millimeter wave region," Opt. Express **26**, 25693 (2018).
11. Z. Lin, X. Pan, J. Yao, Y. Wu, Z. Wang, D. Zhang, C. Ye, S. Xu, F. Yang, and X. Wang, "Characterization of orbital angular momentum applying single-sensor compressive imaging based on a microwave spatial wave modulator," IEEE Trans. Antennas Propag. **26**, 25693 (2021).
12. C. S. Guan, X. M. Ding, Z. C. Wang, K. Zhang, M. Jin, S. N. Burokur, and Q. Wu, "Helicity-switched hologram utilizing a polarization-free multi-bit coding metasurface," Opt. Express **28**, 22669 (2020).
13. Y. Wang, C. S. Guan, X. M. Ding, K. Zhang, B. Ratni, S. N. Burokur, X. M. Gu, and Q. Wu, "Multi-focus hologram utilizing Pancharatnam–Berry phase elements based metamirror," Opt. Lett. **44**, 2189 (2019).
14. Z. C. Wang, J. Liu, X. M. Ding, W. S. Zhao, K. Zhang, H. Y. Li, B. Ratni, S. N. Burokur, and Q. Wu, "Three-dimensional microwave holography based on broadband Huygens' metasurface," Phys. Rev. Appl. **13**, 014033 (2020).
15. Z. C. Wang, X. M. Ding, K. Zhang, B. Ratni, S. N. Burokur, X. M. Gu, and Q. Wu, "Huygens metasurface holograms with the modulation of focal energy distribution," Adv. Opt. Mater. **6**, 1800121 (2018).
16. X. Ding, Z. Wang, G. Hu, J. Liu, K. Zhang, H. Li, B. Ratni, S. N. Burokur, Q. Wu, J. Tan, and C.-W. Qiu, "Metasurface holographic image projection based on mathematical properties of Fourier transform," PhotoniX **1**, 16 (2020).
17. C. Guan, J. Liu, X. Ding, Z. Wang, K. Zhang, H. Li, M. Jin, S. N. Burokur, and Q. Wu, "Dual-polarized multiplexed meta-holograms utilizing coding metasurface," Nanophotonics **9**, 3605 (2020).
18. B. Ratni, Z. Wang, K. Zhang, X. Ding, A. de Lustrac, G.-P. Piau, and S. N. Burokur, "Dynamically controlling spatial energy distribution with a holographic metamirror for adaptive focusing," Phys. Rev. Appl. **13**, 034006 (2020).
19. W. T. Chen, A. Y. Zhu, V. Sanjeev, M. Khorasaninejad, Z. Shi, E. Lee, and F. Capasso, "A broadband achromatic metalens for focusing and imaging in the visible," Nat. Nanotechnol. **13**, 220 (2018).
20. S. Shrestha, A. C. Overvig, M. Lu, A. Stein, and N. Yu, "Broadband achromatic dielectric metalenses," Light: Sci. Appl. **7**, 85 (2018).
21. A. Ndao, L. Hsu, J. Ha, J. H. Park, C. Chang-Hasnain, and B. Kanté, "Octave bandwidth photonic fishnet-achromatic-metalens," Nat. Commun. **11**, 3205 (2020).
22. B. Ratni, A. de Lustrac, G.-P. Piau, and S. N. Burokur, "Reconfigurable metamirror for wavefronts control: applications to microwave antennas," Opt. Express **26**, 2613 (2018).
23. R. Feng, B. Ratni, J. Yi, Z. Jiang, H. Zhang, A. Lustrac, and S. N. Burokur, "Flexible manipulation of Bessel-like beams with a reconfigurable metasurface," Adv. Opt. Mater. **8**, 2001084 (2020).
24. A. de Lustrac, B. Ratni, G. P. Piau, Y. Duval, and S. N. Burokur, "Tri-state metasurface-based electromagnetic screen with switchable reflection, transmission, and absorption functionalities," ACS Appl. Electron. Mater. **3**, 1184 (2021).
25. V. Popov, B. Ratni, S. N. Burokur, and F. Boust, "Non-local reconfigurable sparse metasurface: efficient near-field and far-field wavefront manipulations," Adv. Opt. Mater. **9**, 2001316 (2021).
26. R. Feng, B. Ratni, J. Yi, K. Zhang, X. Ding, H. Zhang, A. de Lustrac, and S. N. Burokur, "Versatile airy-beam generation using a 1-bit coding programmable reflective metasurface," Phys. Rev. Appl. **14**, 014081 (2020).
27. J. Ding, N. Xu, H. Ren, Y. Lin, W. Zhang, and H. Zhang, "Dual-wavelength terahertz metasurfaces with independent phase and amplitude control at each wavelength," Sci. Rep. **6**, 34020 (2016).
28. J. Y. Yan, Y. G. Guo, M. P. Pu, X. L. Li, X. M. Ma, and X. L. Luo, "High-efficiency multi-wavelength metasurface with complete independent phase control," Chin. Opt. Lett. **16**, 050003 (2018).
29. T. Wang, R. Xie, S. Zhu, J. Gao, M. Xin, S. An, B. Zheng, H. Li, Y. Lin, H. Zhang, G. Zhai, and J. Ding, "Dual-band high efficiency terahertz meta-devices based on reflective geometric metasurfaces," IEEE Access **7**, 58131 (2019).
30. R. Xie, M. Xin, S. Chen, D. Zhang, X. Wang, G. Zhai, J. Gao, S. An, B. Zheng, H. Zhang, and J. Ding, "Frequency-multiplexed complex-amplitude meta-devices based on bispectral 2-bit coding meta-atoms," Adv. Opt. Mater. **8**, 2000919 (2020).
31. J. P. B. Mueller, N. A. Rubin, R. C. Devlin, B. Groever, and F. Capasso, "Metasurface polarization optics: independent phase control of arbitrary orthogonal states of polarization," Phys. Rev. Lett. **118**, 113901 (2017).
32. T. Cai, S. Tang, G. Wang, H. Xu, S. Sun, Q. He, and L. Zhou, "High-performance bifunctional metasurfaces in transmission and reflection geometries," Adv. Opt. Mater. **5**, 1600506 (2017).
33. H.-X. Xu, L. Han, Y. Li, Y. Sun, J. Zhao, S. Zhang, and C.-W. Qiu, "Completely spin-decoupled dual-phase hybrid metasurfaces for arbitrary wavefront control," ACS Photon. **6**, 211 (2018).
34. H. X. Xu, G. Hu, M. Jiang, S. Tang, Y. Wang, C. Wang, Y. Huang, X. Ling, H. Liu, and J. Zhou, "Wavevector and frequency multiplexing performed by a spin-decoupled multichannel metasurface," Adv. Mater. Technol. **5**, 1900710 (2019).
35. Y. Y. Yuan, K. Zhang, X. M. Ding, B. Ratni, S. N. Burokur, and Q. Wu, "Complementary transmissive ultra-thin meta-deflectors for broadband polarization-independent refractions in the microwave region," Photon. Res. **7**, 80 (2019).
36. C. Zhang, X. Y. Cao, J. Gao, S. J. Li, H. H. Yang, T. Li, and D. Zhang, "Shared aperture metasurface for bi-functions: radiation and low backward scattering performance," IEEE Access **7**, 56547 (2019).
37. Y. Yuan, S. Chen, B. Ratni, Q. Wu, X. Ding, S. N. Burokur, and K. Zhang, "Bi-functional meta-device with full energy utilization in co-and cross-polarization fields," Appl. Phys. Lett. **117**, 171602 (2020).
38. Y. Yuan, K. Zhang, B. Ratni, Q. Song, X. Ding, Q. Wu, S. N. Burokur, and P. Genevet, "Independent phase modulation for quadruplex polarization channels enabled by chirality-assisted geometric-phase metasurfaces," Nat. Commun. **11**, 4186 (2020).
39. K. Zhang, Y. Yuan, X. Ding, H. Li, B. Ratni, Q. Wu, J. Liu, S. N. Burokur, and J. Tan, "Polarization-engineered noninterleaved metasurface for integer and fractional orbital angular momentum multiplexing," Laser Photon. Rev. **15**, 2000351 (2020).
40. S. M. Kamali, E. Arbabi, A. Arbabi, Y. Horie, M. S. Faraji-Dana, and A. Faraon, "Angle-multiplexed metasurfaces: encoding independent wavefronts in a single metasurface under different illumination angles," Phys. Rev. X **7**, 041056 (2017).
41. M. Qiu, M. Jia, S. Ma, S. Sun, Q. He, and L. Zhou, "Angular dispersions in terahertz metasurfaces: physics and applications," Phys. Rev. Appl. **9**, 54050 (2018).
42. E. Wang, J. Niu, Y. Liang, H. L. Li, Y. Hua, L. Shi, and C. Xie, "Complete control of multichannel, angle-multiplexed, and arbitrary spatially varying polarization fields," Adv. Opt. Mater. **8**, 1901674 (2020).
43. L. Wang, Y. Yang, L. Deng, W. Hong, C. Zhang, and S. Li, "Terahertz angle-multiplexed metasurface for multi-dimensional multiplexing of spatial and frequency domains," Adv. Theory Simul. **3**, 2000115 (2020).
44. C. Huang, Y. J. Feng, J. M. Zhao, Z. B. Wang, and T. Jiang, "Asymmetric electromagnetic wave transmission of linear polarization via polarization conversion through chiral metamaterial structures," Phys. Rev. B **85**, 195131 (2012).
45. K. Chen, G. W. Ding, G. W. Hu, Z. W. Jin, J. M. Zhao, Y. J. Feng, T. Jiang, A. Alu, and C. W. Qiu, "Directional Janus metasurface," Adv. Mater. **32**, 1906352 (2020).
46. B. S. Yao, X. F. Zang, Z. Li, L. Chen, J. Y. Xie, Y. M. Zhu, and S. L. Zhuang, "Dual-layered metasurfaces for asymmetric focusing," Photon. Res. **8**, 830 (2020).